ATLAS Internal Note
CAL-NO-067
15 January 1995

Performance of a Liquid Argon Electromagnetic Endcap Calorimeter using an Accordion Geometry

A.Chekhtman, P.Fassnacht, D.Fouchez and E.Monnier
Centre de Physique des Particules de Marseille,
F-13288 Marseille, France

L.Serin
Laboratoire de l'Accélérateur Linéaire et Université de Paris-Sud,
F-91405 Orsay, France

Abstract

The design and construction of a lead-liquid argon Endcap calorimeter prototype using an accordion geometry is described. The performances obtained using electron beam data are presented. The results are compared to the one obtained with a barrel prototype designed with the same concept of accordion geometry and are found to be very similar: an energy resolution with a sampling term below $11\%/\sqrt{E(GeV)}$ and a small local constant term, a linearity better than $\pm$ 0.5% and an overall constant term of 0.8% over an extended area in the rapidity range of $2.2 < \eta < 2.9$.

1 Introduction

Several physics studies [1] [2] showed that the Endcap calorimeter must have similar performances as the Barrel. It has been therefore decided to study the performances of a liquid argon Endcap calorimeter using the same concept of accordion geometry as the barrel part [3]. Encouraged by the success in the design, the construction and the operation of the 2m barrel prototype, we have adapted the same technology to the design and the construction [4] of the Endcap module. The adapted geometry ensured a high degree of hermeticity of the calorimeter. A prototype has been designed, built and exposed to electrons with energies between 20 to 300 GeV in the H8 beam line of the CERN SPS. In the following sections we describe the prototype, the test beam setup used and the measured performances. Emphasize is put on the differences with respect to the barrel design and on the comparison with the barrel performances.

2 Detector description

The prototype has been designed as a sector of an inner wheel of the ATLAS Endcap calorimeter [2]. It consists of a sixth of a full wheel nominally built out of 348 converters and as many kapton readout boards. All the plates (converters and kaptons) are accordion shaped and are arranged radially like wheel spokes with the waves parallel to the beam axis. This calorimeter module form a part of a flat disk perpendicular to the beam axis with readout cells, located on the kapton boards, pointing in both η and ϕ directions to a "vertex" located at 2.8 m from the front face. The detector geometry corresponds to a rapidity coverage from 2.16 to 2.88, divided into 24 strips of constant $\Delta\eta = 0.03$. In azimuth three strips from consecutive kapton boards are ganged together and thus define cells with a constant $\Delta\phi = 0.05$. Each strip has a longitudinal segmentation in three depth regions of $9X_o, 9X_o$ and $6X_o$ close to the one used for the 2m barrel prototype. Therefore, readout cells are defined with $\Delta\eta \times \Delta\phi = 0.03 \times 0.05$ for the two first sampling depth regions. For the third depth region, η strips are larger by a factor two and thus define cells with $\Delta\eta \times \Delta\phi = 0.06 \times 0.05$. The pointing structure in ϕ is achieved by opening up the absorber and readout plates along the beam line (Fig. 1). This leads to a variation of all the accordion parameters along the radius (η direction) : the (bi)gap increases from 3.9 to 5.3 mm with the radius and, in order to keep the sampling fraction constant in both η and ϕ direction, the lead sheet thickness increases from 1.3 to 2.3 mm and the wave angle decreases from 57^o to 110^o.

The correspondence between the cells coordinates N_η and the η values in the ATLAS detector configuration is given in table 1.

Constant response, at short shaping, is obtained provided the drift time is also constant. This is achieved, in first approximation, by increasing the HV radially, by groups of 2 strips in η, independently for the first depth region and for both the second and third ones (both connected at the same HV). Thus, in our standard operating conditions, twelve different voltages for the first sampling zone and twelve others for the second and third zones were defined. They ranged typically from 1000 V at low radius to 2500 V at the largest. Their fine tuning is defined in section 4.3.1.

This variation of the HV along η and the continuous variation of the detector geometry along this direction are the major differences with respect to the barrel design.

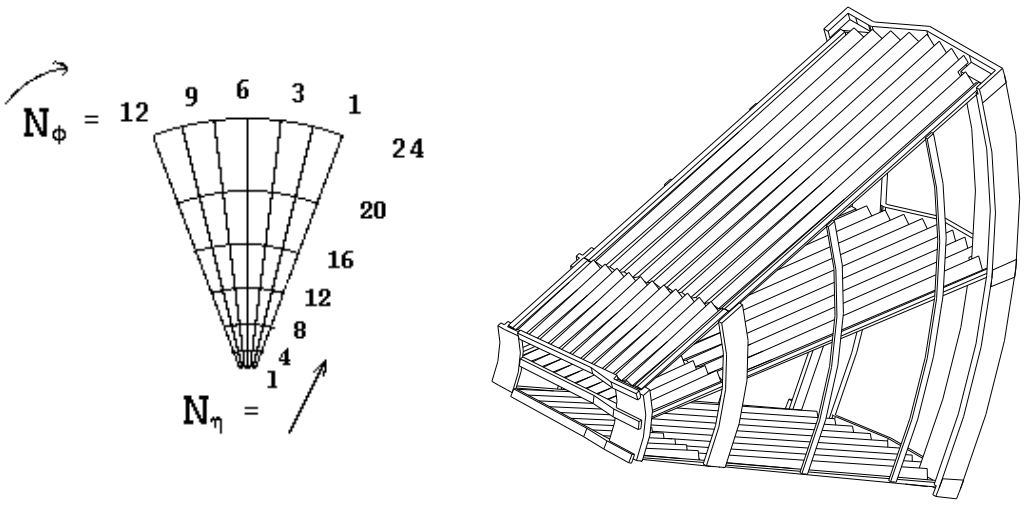

Figure 1: *On the left : System of coordinates on the front face of the prototype, in cell unit. On the right : Sketch of an end-cap module (with its structure) for the ATLAS detector. The prototype corresponds to the inner wheel dimensions (i.e. smaller radius)*

N_η	1	7	10	15	22	24
η	2.88	2.65	2.56	2.42	2.21	2.17

Table 1: *Correspondence between the cell numbering N_η and the η values in the ATLAS detector configuration.*

The production of the converters, using similar techniques as the ones developed for the barrel prototypes, did not show any problems. The CERN bending machine, modified for the Endcaps [4], worked well. The Marseille gluing machine which uses, as a gluing mould, two jaws made of a set of bars identical to the ones of the bending machine, worked fine as well. The theoretical shape was well reproduced using the technical concept which consists to use two identical set of bars for the bending and for the gluing of the converters. A precision on the gap size of a tenth of millimeter has been achieved. In a similar way as for the barrel sector, honeycomb strips, glued to the converter plates in a few points, were used to center the kapton readout electrodes. However, in order to cope with the variable gap between kapton and converter plates, these honeycomb strips had a variable thickness. The assembly of the detector was completed without significant problems.

In order to have a distance between the interaction point and the active readout region close to those specified for a detector at LHC and also to be able to use the same platform to move along η as for the Barrel, it has been chosen to have a simulated interaction point at 2.8m. But the differences in the rotation lever arms (2.8 instead of 1.3 for the Barrel) have to be compensated. This was achieved by putting the calorimeter in the back of the cryostat. Rohacell foam was used as argon excluder. The displacement along ϕ was made with a motor operating in the liquid argon as shown on Fig. 2.

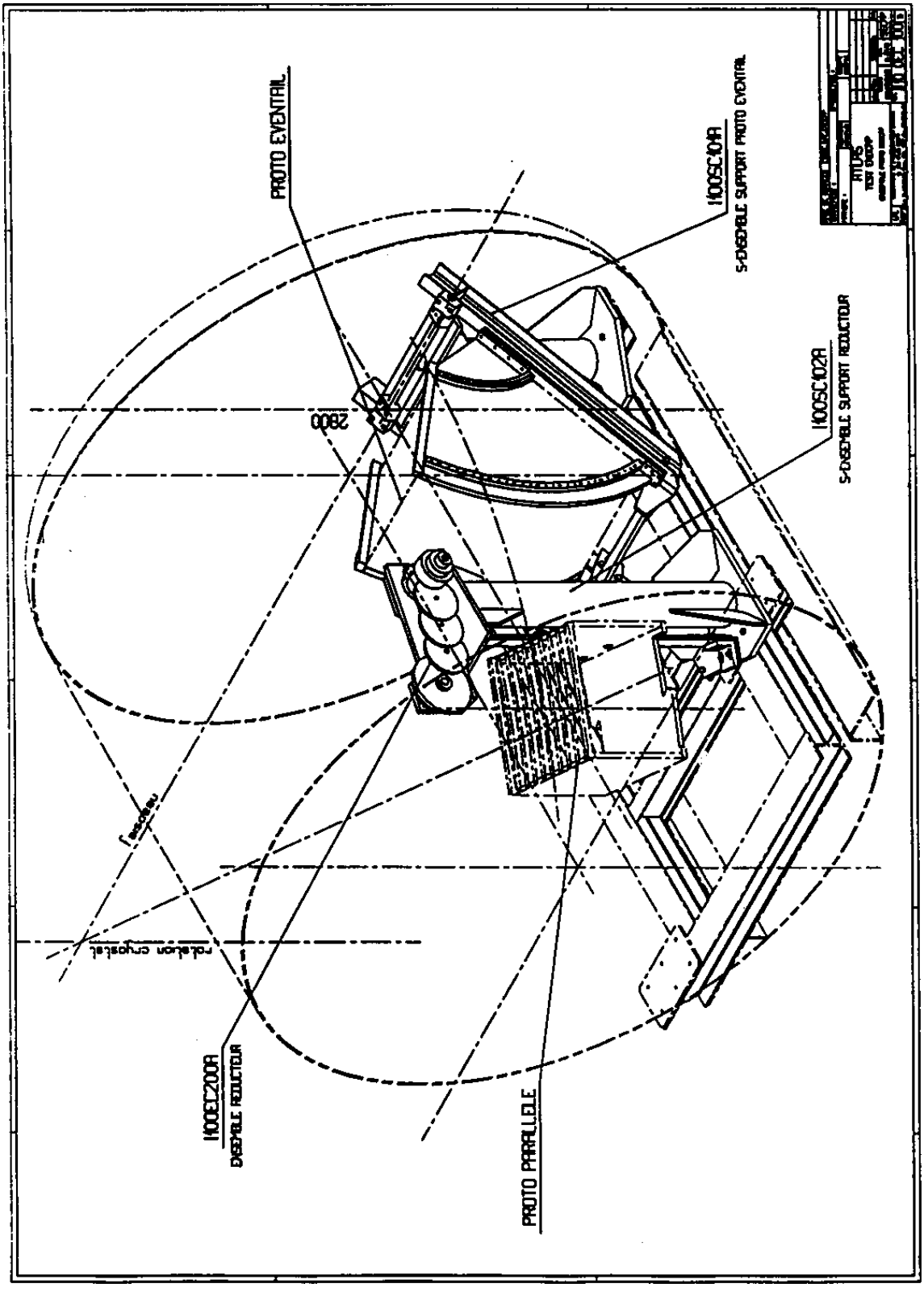

Figure 2: *Test beam setup : Scheme of the prototype (called "PROTO EVENTAIL") inside the cryostat together with the motor used to move along ϕ*

As mentioned previously, the signal read out electrodes are grouped together to form cells. This was achieved on the mother boards plugged onto the kapton foils. Care has been taken in their design to have all the signal strips of a mother board isochronous within 0.1 ns. The preamplifier used are the so called "0T" warm electronics already described in [3] as well as the readout with "Track and Hold" (T&H). Due to the increase of the cell capacitance with respect to the radius, which induces a variation of the peaking time, we have grouped the channels corresponding to six consecutive values in η and four in ϕ on a same T&H. Cables, feedthroughs, and subsequent electronics were those used for the previous tests with the Barrel prototype.

3 Simulation

For the simulation of the Endcap prototype performances, a GEANT based Monte Carlo (MC) program has been written. It contains the detailed description of the detector geometry where all the parameters of the accordion shape: opening angles, thicknesses of the absorbers and gaps between the absorbers and the electrodes - depend on the distance from the detector axis.

The simulation also takes into account the effects of charge collection, the non-uniformity of the electric field in the folded region and the dependence of the high voltage versus the η value of a cell. It also reproduces correctly the division of the prototype into the three samplings and the projective cells in the η direction.

The simulation gave the following results :

- A correlation was found between the total energy deposition in the calorimeter and the energy in the third sampling (Fig. 3). This shows the presence of a backward leakage, which is proportional to the energy deposited in the third sampling. The slope parameter which is equal to 0.3 and independent of the initial electron energy was then used to correct the energy response of the calorimeter.

- Simulated calorimeter response as a function of ϕ has periodical modulations due to two effects : a) non-uniformity of the sampling fraction near the absorber fold and b) non-uniformity of the electric field near the absorber or the electrode fold. The sum of these two effects produces two sets of peaks with different amplitudes and widths at the position of the absorber and the electrode folds (Fig. 4).

- The energy resolution obtained after correction for the ϕ modulations and the backward leakage is shown (Fig. 5) as a function of the initial particle energy. The fit gives a sampling term of 10% and a constant term of 0.25%.

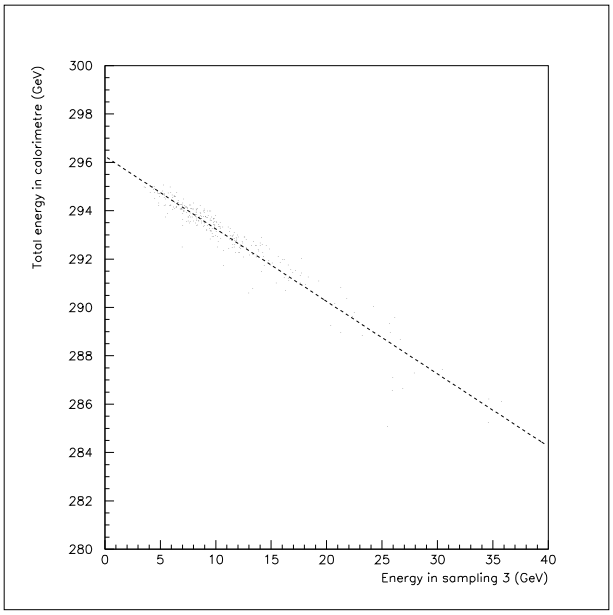

Figure 3: *Correlation between the total energy and the energy in sampling 3 (Monte Carlo data)*

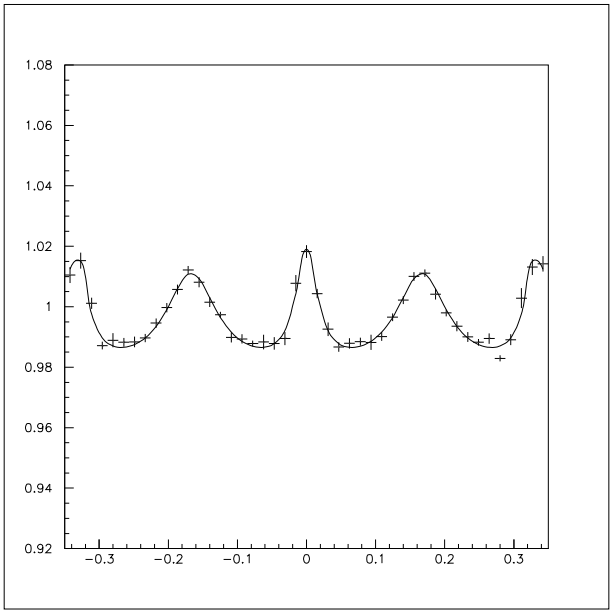

Figure 4: *Modulations of the signal along the ϕ direction (cell unit) (Monte Carlo)*

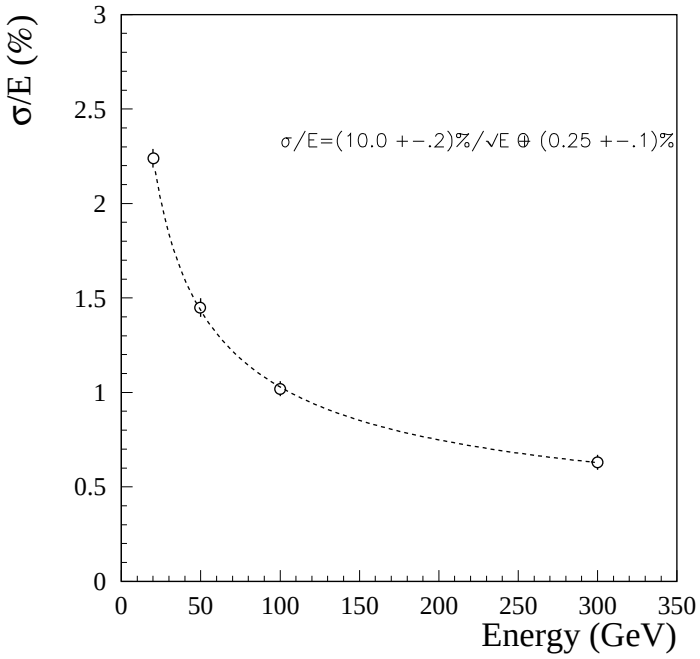

Figure 5: *Energy resolution (Monte Carlo)*

4 Test Beam results

4.1 Test Beam setup

The data have been taken in the H8 beam line of the CERN SPS using electrons of 20, 50, 100, 200 and 300 GeV during two periods, in November 1993 and in April 1994.

The calorimeter was installed inside a cryostat consisting of a 1.2 mm thick aluminium outer wall, followed by a 30 cm low density foam and by a 8 mm thick stainless steel inner vessel. As mentioned in section 2, the calorimeter was put at the back of the cryostat behind 140 cm low density foam, used as argon excluder. The total amount of passive material in front of the prototype was about 0.9 X_0 at η= 2.9.

As described in the section 2, the calorimeter could be rotated in the two η and ϕ directions in order to hit the selected cells along their projective axis.

The beam line was equipped with three proportional wire chambers, which allowed to determine the direction of the incident particles and their impact point on the calorimeter, and with four scintillator counters used to define the spot size and for triggering.

4.2 Performance of the electronic chain

A detailed description of the readout chain and the calibration procedure is given in the barrel description [3].

- Timing

  The calibration and the physic signals must be timed in such a way that the shaper response of each channel is sampled at his maximum by the T&H circuit. During the timing calibration procedure, the peaking time of each channel (i.e. the delay of the maximum of the shaper signal), which varies along the η direction due to capacitance variations, is measured. The measurements for all channels in the first sampling show an η dependence for each group of the six cells on the same T&H and a small dispersion. The resulting distribution has a dispersion of 0.44 ns (after tuning the delays and unfolding the η dependence) (see Fig. 6).

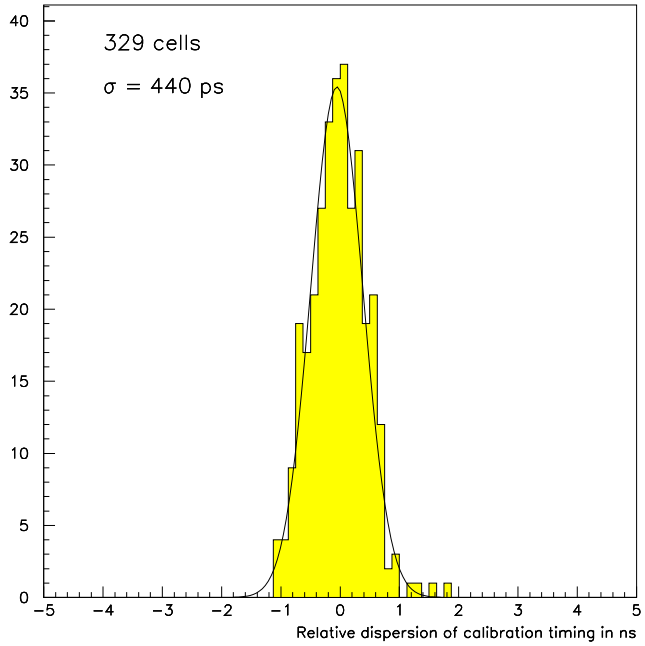

Figure 6: *Peaking time distribution*

- Electronic noise

  The coherent noise, usually associated to improper shielding and ground loops has been measured to be 6 MeV, 6 MeV and 7 MeV per channel in the first, second and third sampling, respectively.

  The uncoherent noise observed in the calorimeter comes mainly from the preamplifier noise and varies with η (capacitance). It has been measured to be between 46 and 52 MeV per channel in the first sampling, between 46 and 56 MeV in the second and third sampling.

- Cross talk

  The cross talk between adjacent cells has been estimated using the calibration data and found to be at the level of 1 % between neighbors. Therefore it has negligible effect on the energy resolution and has not been corrected for.

4.3 Energy response to electrons

The electron shower is reconstructed by summing the cell responses of a 5 (η) $\times$ 3 (ϕ) matrix for the first two sampling and of a 3 (η) $\times$ 3 (ϕ) matrix for the third sampling (where the granularity is twice coarser). This corresponds to a front calorimeter window of about 6 $\times$ 6 cm^2 (12 $\times$ 12 cm^2) at the lowest (highest) radius. The energy containment was of the order of 95%.

4.3.1 High Voltage adjustment

As explained in section 2, the high voltage has to be increased radially (i.e. along the η direction) to keep the response of the calorimeter constant. An initial set of theoretical values has been obtained from the Monte Carlo simulation. To check this first setting, we have scanned the whole range in η with 200 GeV electrons. A slope of the order of a few percent has been found and the HV values have then been adjusted online according to this slope in order to obtain an overall flat response. This difference between MC and real data can be easily explained by uncertainties on the theoretical drift velocity.

Since HV is distributed by pairs of adjacent cells, we expect to see a fine radial dependence for each pair of two consecutive cells in the η direction : for one cell of the pair the signal will be over-estimated and under-estimated for the other one. Such a feature clearly appears in the data : the energy response of each cell has been represented on Fig. 7 after normalization (on the mean response of each pair of cells at same HV). One can see the corresponding 'HV effect' affecting the odd and even cells.

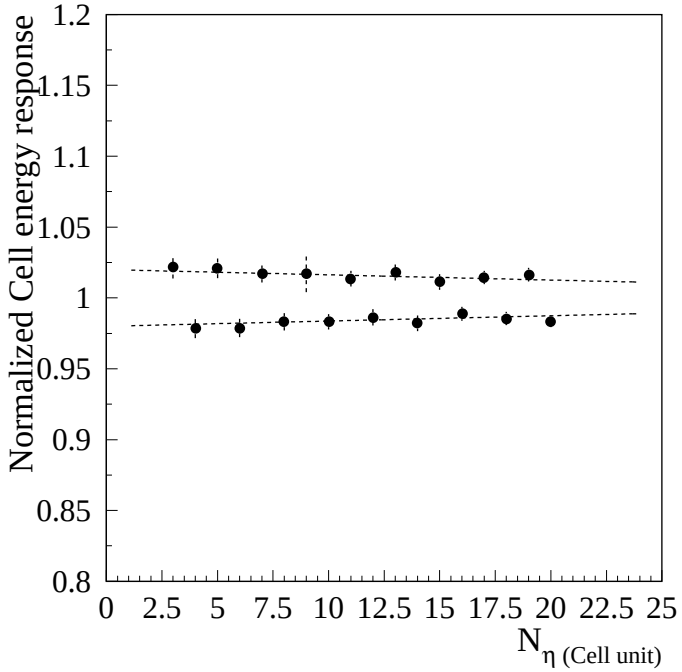

Figure 7: *Normalized signal as a function of the cell number. HV effect on odd-even cells (see text). The two dotted lines correspond to a linear fit on the odd and even cells response.*

This effect is in agreement with the behaviour observed in the MC data. We use two different linear functions : one for even cells and one for odd cells, to compute 'HV correction' coefficients (see Fig. 7).

These coefficients were then applied to correct offline the response of each cell at a given η.

4.3.2 Response variation across a cell

We studied the calorimeter response versus the impact point inside a cell. The impact point is computed from the energy barycenter of the electromagnetic shower (see section 4.4). The variations inside a cell in both the η and ϕ directions are expected to be the same as those found for the barrel and will be corrected in a similar way. However, as mentioned before, the parameters of the detector geometry (which mainly determine these variations) change with η. We therefore looked at the behaviour of these variations along the radius for different cells in η.

- Versus η

  The response w.r.t. η of the Endcap prototype inside a window is shown on the left hand side of Fig. 8 for various N_η cell positions. The typical parabolic shape reflects lateral leakage and the separation between two cells. It has been parametrized by the following function :

  $$\alpha.\eta^{'} + \beta.\eta^{'2} + \gamma.\eta^{'4}$$

  where $\eta^{'} = \eta$ modulo(cell size)

  No sensitive 'radial' dependence has been found for this correction, and a constant correction has been used over the full η range in the following results.

- Versus ϕ

  The response w.r.t ϕ is shown on the right hand side of Fig 8. The different profiles show some modulations corresponding to the accordion shape. They were parametrized using the following periodic function (same as the one used for the Monte Carlo data, see section 3) :

  $$\frac{A}{1+(\phi'-B)^2} + \frac{C}{1+(\phi'-D)^2} + E.\phi^{'2}$$

  where $\phi^{'} = \phi$ modulo(cell size/3)

  A small radial dependence of this correction has been observed but no parametrization has been computed. Nevertheless a local correction (i.e. suited for each radius) has been applied in the determination of the energy resolution (see 4.3.4).

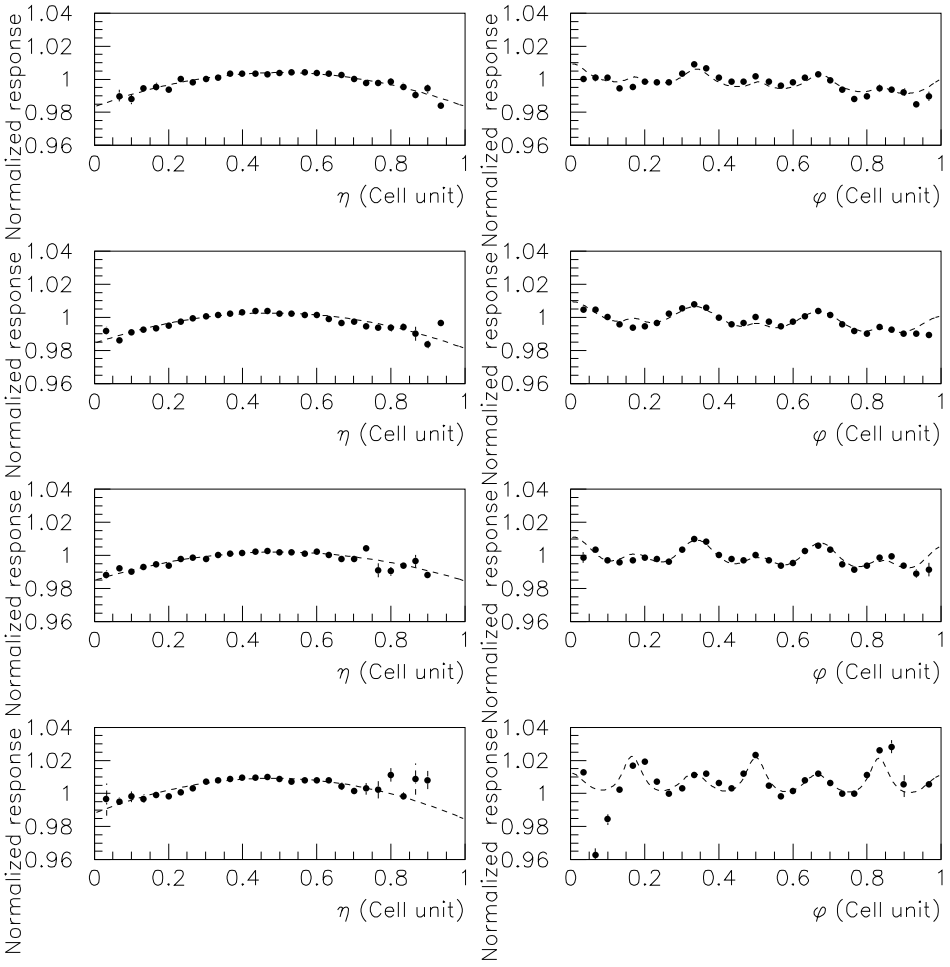

Figure 8: *Normalized energy response versus η and ϕ inside a cell for 4 different cells : N_η = 7,10,15 and 22 (from top to bottom)*

4.3.3 Longitudinal leakage and shower depth dependence

As the total calorimeter length is 24 X_o, there is a longitudinal leakage which is not negligible in terms of energy resolution at high energy.

The energy deposited in the third sampling compartment can be used to determine this leakage. The Monte Carlo simulation shows that there is a linear dependence that can be parametrized by : $E_{tot} = E_{calo} + 0.3.E_{s3}$ (see section 3). This formula will be used in the following analysis to compute the total energy (where an improvement of 0.2% of the energy resolution at 300 GeV is obtained with this correction).

The calorimeter response as a function of the shower depth, i.e. the longitudinal barycenter defined as $(\sum_{i=1,3} E_{s_i}.x_{s_i})/(\sum_{i=1,3} E_{s_i})$ where i is the sampling number and $x_{s_i} = i - \frac{1}{2}$, is shown in Fig. 9. There is a depletion when the shower maximum energy is in the first part of the calorimeter. This depletion is corrected by a polynomial function fitted to the data. This behaviour can be explained by the energy losses in front of the calorimeter for early developed shower (see next section).

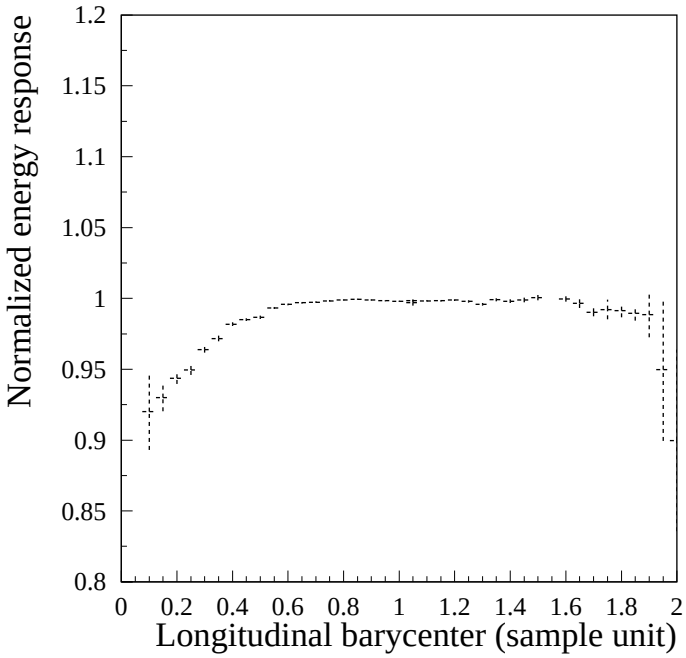

Figure 9: *Normalized energy response versus the longitudinal barycenter of the shower*

4.3.4 Energy resolution

The data have been collected for four different values in η and two in ϕ. The energy is computed inside a 5×3 window and corrected for the non-uniformity in both η (clustering effect) and ϕ (modulation) directions as describe in section 4.3.2. The corrections corresponding to the leakage and shower depth are also applied. No contribution from the beam energy spread has been unfolded to compute the energy resolution. A typical distribution corresponding to electrons of 300 GeV incident energy is shown on Fig. 10. It shows a gaussian response with only few events in the tail. The gaussian fit gives a resolution σ/E of 0.7%.

The energy resolution as a function of the beam energy, has been computed for four different η values. The different points are shown on Fig. 11.

At a given η value, the energy resolution values we obtained were parametrized with the following quadratic sum:

$$\frac{\sigma_E}{E} = \frac{a}{\sqrt{E}}\% \oplus \frac{b}{E} \oplus c\%$$

where the three terms are the sampling, the noise and the local constant term respectively and E is expressed in GeV. The values of the three coefficients, for the four different cell numbers (N_η), are given in table 2.

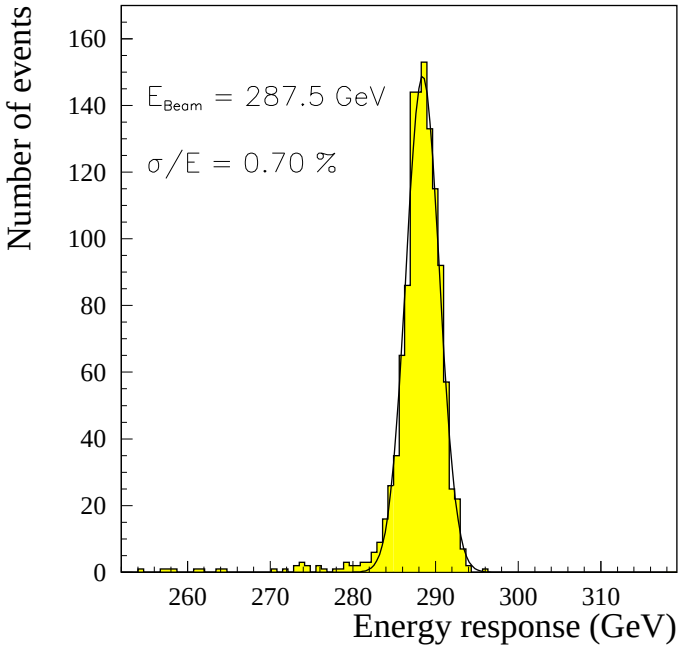

Figure 10: *Reconstructed energy spectrum in the calorimeter for 300 GeV electrons. The full line is a gaussian fit.*

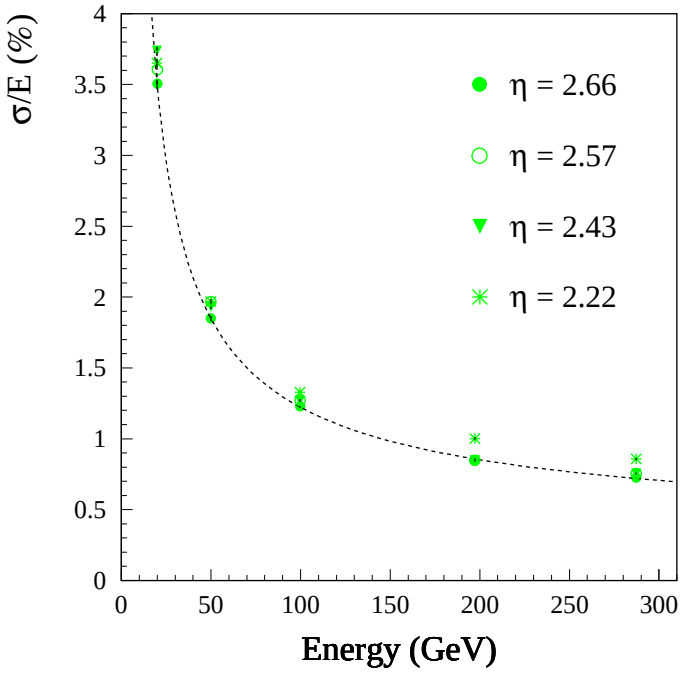

Figure 11: *Energy resolution as a function of the incident beam energy at four different η values. The dashed line is the best fit to the data at η=2.66*

η [Cell number]	a: Sampling term (% $GeV^{-\frac{1}{2}}$)	b: Noise term (MeV)	c: Constant term (%)
2.66 [7]	10.7 ($\pm$ .3)	507 ($\pm$ 18)	.30 ($\pm$.04)
2.57 [10]	11.1 ($\pm$ .3)	534 ($\pm$ 21)	.28 ($\pm$.04)
2.43 [15]	10.6 ($\pm$ .2)	573 ($\pm$ 15)	.35 ($\pm$.03)
2.22 [22]	11.4 ($\pm$ .3)	507 ($\pm$ 18)	.51 ($\pm$.03)

Table 2: *Energy resolution fit parameters for the four various η values*

The sampling term (a) is of the order of 10-11%, in good agreement with the simulation and with the value obtained for the barrel. The noise term (b) has been checked using random triggers and was found to be larger than the electronic noise by about 70-100 MeV. The constant term (c) reflects mainly the residual modulations in both ϕ and η directions.

If we exclude the point at N_η=22 (where an additional non-uniformity is suspected, see section 4.6), the η dependence of the energy resolution is not significant in the sampling term and in the constant term. The noise term depends slightly on η due to the increase of the capacitance.

To study the effect of the material in front of the calorimeter, one can use the preshower information. The preshower in front of the prototype consists of only one plane of pads without any absorbers and is located at 1.4 meters from the cryostat wall. It has been used as a veto.

The noise term contribution to the energy resolution at 20 GeV versus different cuts on the preshower signal is shown on Fig. 12. We assumed that the sampling term and the constant term are independent of the preshower cut. This has been confirmed at 300 Gev where the noise term is negligible and the resolution almost unchanged for the same preshower cuts. The noise term after the cut on the preshower signal becomes now compatible with the expected electronic noise. Clearly, the material in front of the calorimeter degrades the resolution, especially at low energy, which in the fit procedure reflects in an increased noise term.

4.3.5 Linearity

The linearity has been studied with the same data used to determine the energy resolution. The pedestal value, extracted from the events triggered randomly, is subtracted from the mean value of the fitted calorimeter response. The resulting value is then divided by the nominal beam energy (and normalized at 100 GeV). The linearity is better than $\pm$ 0.5% at the four selected η values (see Fig. 13)

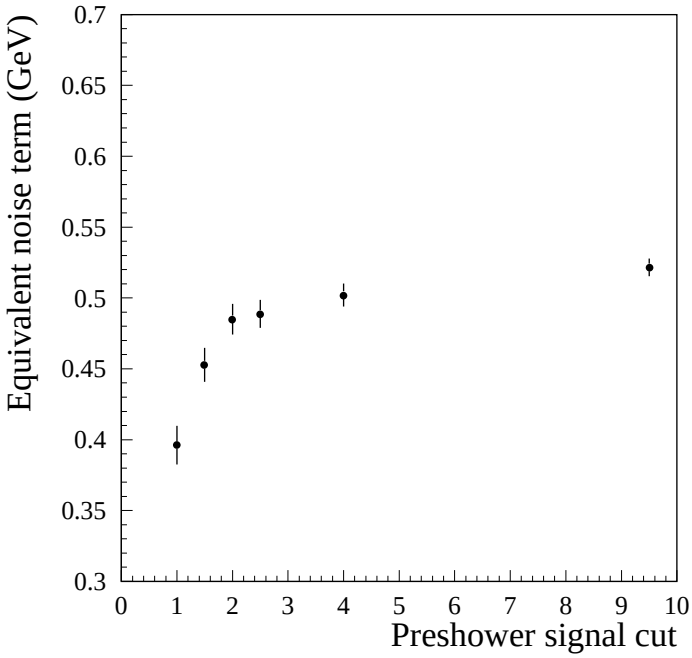

Figure 12: *Energy resolution at 20 GeV in equivalent noise term versus the preshower signal cut*

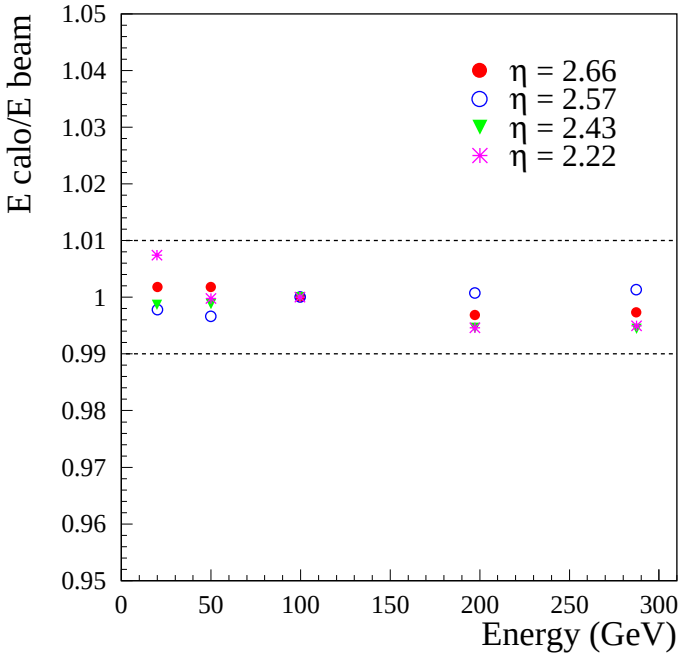

Figure 13: *Linearity of the calorimeter response for four different cells in η*

4.4 Position resolution

The calorimeter position, in both η and ϕ directions, is determined by the energy weighted barycenter of the 3×3 cell cluster. The resolution in position, calculated only in the first sampling, is obtained by the difference with respect to the impact point reconstructed using the three beam chambers.

The different behaviour of the Endcap prototype along the two directions is shown in Fig. 14 where the positions reconstructed by the calorimeter are compared to the ones obtained using the beam chamber informations. In the ϕ direction a linear fit describes well enough the correlation whereas in the η direction a tangent function has been used to correct for the correlation.

Along the η direction (see Fig. 15), the r.m.s. of the distribution at large radius ($N_\eta = 22$) is 465.±26.μm for 300 GeV electrons, including the beam chamber resolution which is $\simeq$ 250 μm for E_{beam} $\geq$50 GeV and $\simeq$ 400μm at E_{beam}=20 GeV. Unfolding this latter contribution, we obtain a spatial resolution of 415.±28.μm at 300 GeV. This value was obtained without any cut to remove possible edge effects which can be observed on Fig. 15 where $X_{calo} - X_{chs}$ has been plotted as a function of the position in the cell. A clear improvement of the resolution is observed when going to the edges of the cell.

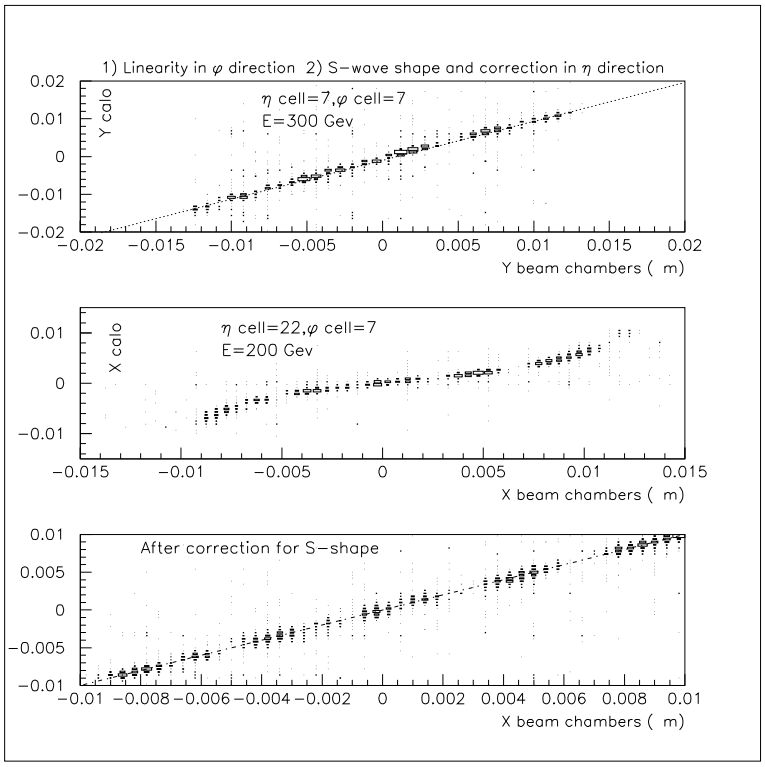

Figure 14: *Calorimeter coordinates versus coordinates extrapolated using beam chambers*

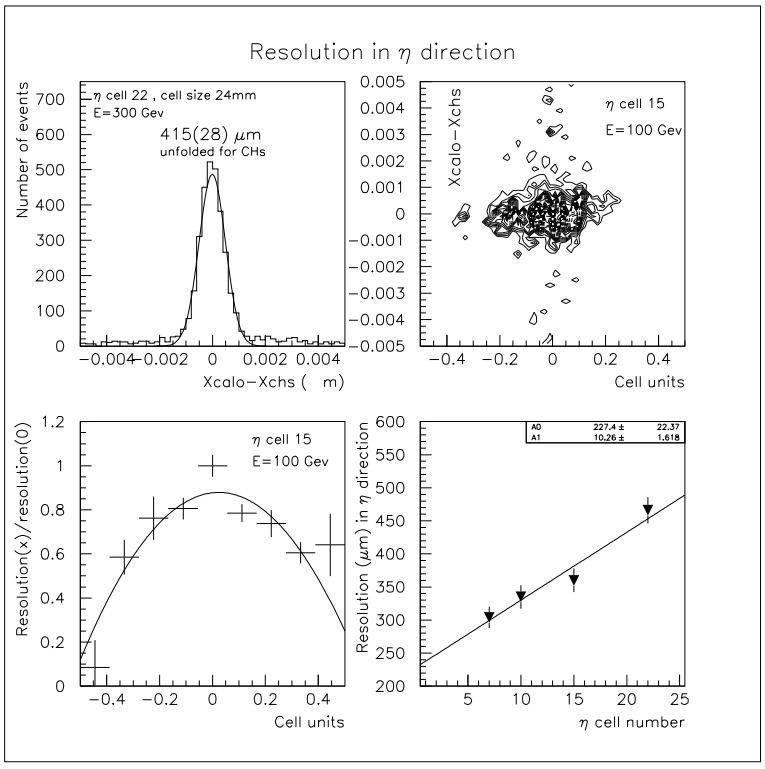

Figure 15: *Resolution in the η direction*

Finally, the variation of the resolution with the radius has been plotted on the same figure. A clear dependence, corresponding to an increase of the resolution of $10.3 \pm 1.6 \mu$m per cell, has been observed. Between the innermost and the outermost radii, the resolution raised from 230μm to 450μm. Such a variation, directly related to the increase of the cell size by a factor of two, is well understood since the resolution is proportional to the cell size [3].
The dependence of the position resolution in the η direction with the incident beam energy has been obtained for five different values : 20, 50, 100, 200 and 300 GeV. The variation versus $\frac{1.}{\sqrt{E}}$ is shown in Fig. 16 for three different values in η (cell number 7, 15 and 22). The measured values have been fitted by the quadratic sum :

$$\sigma(mm) = A0 \oplus \frac{A1}{\sqrt{E(GeV)}} \oplus \frac{A2}{E(GeV)}$$

The following table shows the different values taken by those three parameters for the three different cell numbers. A0 (constant term) and A2 (noise term) does not show a dependence w.r.t. the radius whereas such a dependence is observed for the sampling term (A1).

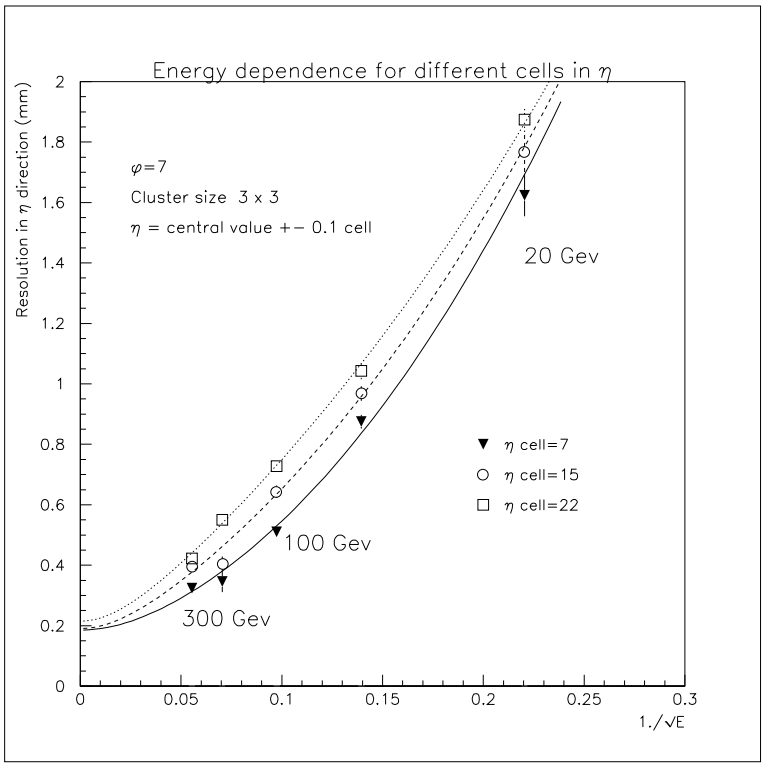

Figure 16: *Resolution versus energy in the η direction*

Concerning the sampling term as well as the constant term, these values are in good agreement with the one obtained for the 2m barrel prototype [2]. The noise term is somewhat larger than the one obtained for the 2m prototype. This increased noise term found in the fit procedure is explained by the scattering of the electrons in the cryostat wall located at 140 cm from the calorimeter front face (see 4.1).

η cell number	A0 (mm)	A1 (mm $GeV^{-1/2}$)	A2 (mm GeV^{-1})
7	.185±.047	4.25±.47	28.7±2.7
15	.237±.054	6.07±.47	19.3±4.1
22	.215±.052	6.83±.35	22.1±2.9

The resolution has also been measured in the ϕ direction for different values in η in order to study how the resolution is affected by the cell size, which varies as mentioned by a factor of two going along the radius. At cell N_η=7 a resolution in the ϕ direction of 390.±20.μm (corrected for chamber resolution, which is the same as in the η direction) has been obtained, as shown on Fig. 17. No variation w.r.t. the position within a given cell has been observed, but as in the η direction, a clear variation of the resolution with increasing radius has been observed. This variation (Fig. 17) shows a corresponding slope of 9.7±2.2 μm per cell, comparable to the one found in the η direction.

Finally, the energy dependence at cell (N_η=10,N_ϕ=7) has been measured. Fig. 17 shows the resolution measured versus $\frac{1.}{\sqrt{E}}$. The values of A0 and A2 are essentially the sames as it was obtained in the η direction. The sampling term A1, compared at same cell size in the two directions, is lower by $\simeq$ 40% in the ϕ direction. In order to compare these values to those obtained with the barrel (i.e. with a cell size of 2.5 cm in η and 2.7 cm in ϕ), the values

of the resolution in both directions have been taken at the proper radii, corresponding to N_η = 23 and 6 respectively. The ratio of the corresponding resolution values along η over the resolution along ϕ was found to be 1.6$\pm$0.3, indicating a better resolution in the ϕ direction. That value is well in agreement with the equivalent ratio reported for the barrel [2].

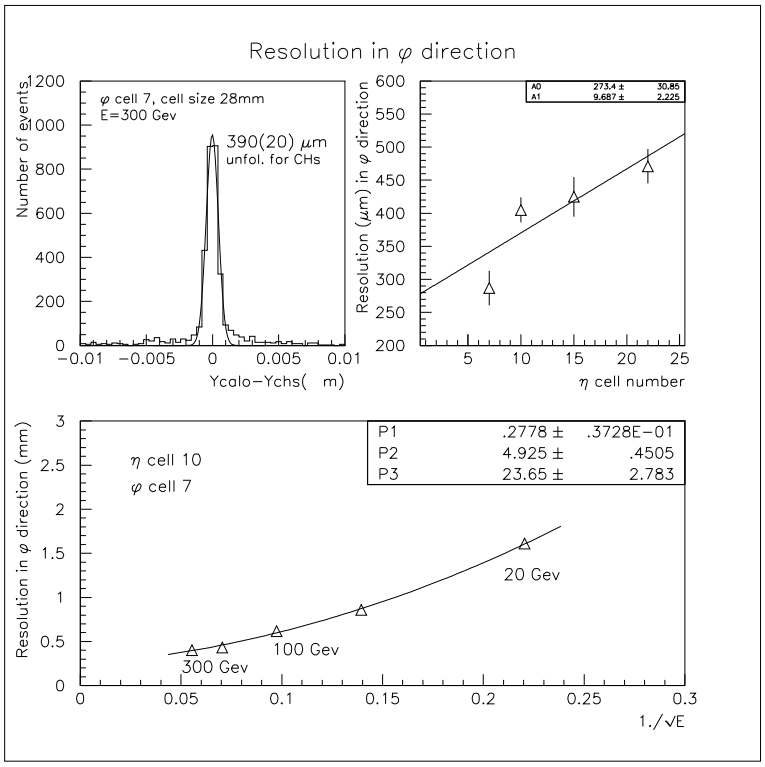

Figure 17: Resolution in the ϕ direction

4.5 Response uniformity

Response uniformity has been studied in both η and ϕ directions with dedicated sets of data, using 200 GeV and 300 GeV electrons.

Three lines covering the η range at three different ϕ positions are used to test the uniformity along the η direction and two lines covering the ϕ range at two different η positions are used to test the uniformity along ϕ.

The complete scan of the Endcap prototype could not be achieved because of some dead or non-equipped regions: the detector showed a non-continuity in the HV distribution between two kaptons at N_ϕ=2 and N_ϕ=3 in the region N_η = 3-4 ; the region N_ϕ = 14, 15 and 16 was not equipped with readout electronics and a dead channel was located at (N_η=6,N_ϕ=11). As a consequence, and because of the size of the window (5 cells in η, 3 cells in ϕ), the η coverage for the scan will be restricted to [7-22] and the ϕ coverage to the range [2-12] at N_η=15 and [2-9] at N_η=7.

4.5.1 Response Uniformity versus η

The normalized energy response to 200 GeV electrons versus η is shown in Fig. 18 for 3 different cluster sizes. The data corresponding to the 5×3 cluster are used to determine the correction for non-uniformity. We observe a global linear variation corresponding to the increase of the cell size with η and a local parabolic shape for each cell as described in section 4.3.2.

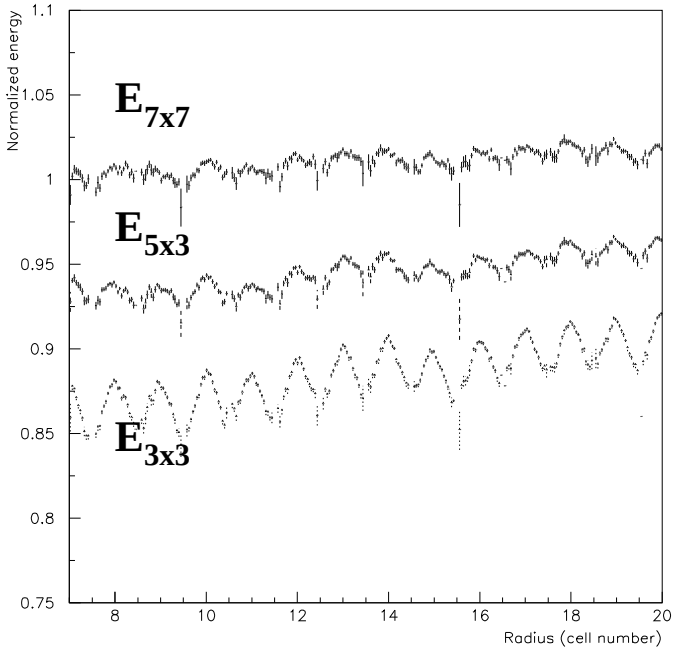

Figure 18: *Calorimeter response along a radius*

We first use a linear correction to correct for the first effect. Next, by summing all the data of same $\delta\eta$ (where $\delta\eta = \eta$ modulo(cell size)), we compute a parabolic correction and a ϕ modulation correction functions (see section 4.3.2). As mentioned in section 4.3.2 no global η dependence for the local parabolic correction and ϕ modulation has been used.

Using those corrections, we obtained the normalized energy response as a function of N_η, for a total of 48 cells (Fig. 19) corresponding to three different values of ϕ. The global dispersion of those points is $0.55(\pm.08)\%$. We can see a remaining systematic effect along the η direction for each ϕ value. This effect will be studied in section 4.6

The mean resolution obtained for the three lines (16 cells at N_ϕ=constant) is equal to 1.05%. Subtracting from that value the measured contribution of the sampling term (0.76%) and noise term (0.26%) at 200 GeV, we obtain a constant term of 0.66% along η.

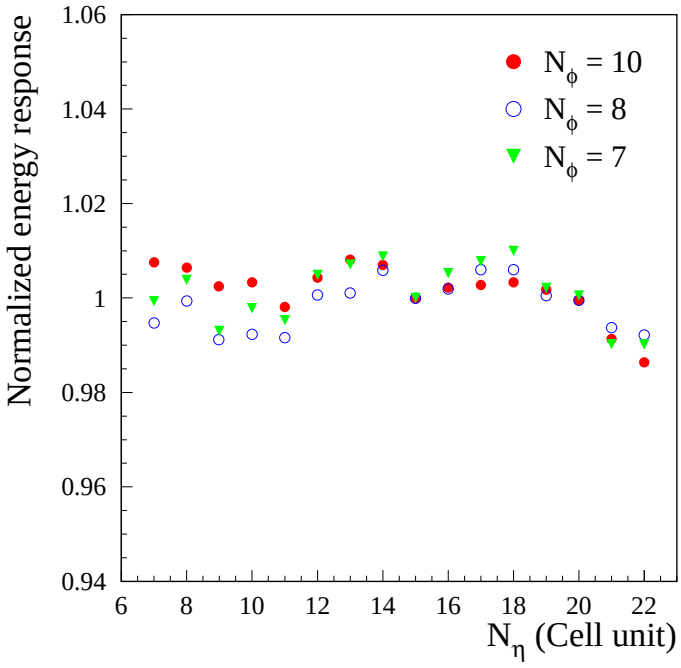

Figure 19: *Uniformity along the η direction for three different values in ϕ*

4.5.2 Response Uniformity versus ϕ

The energy response to 300 GeV electrons as a function of ϕ is shown in Fig. 20 for N_η=15. One clearly observe some modulations over the five consecutive cells.

As in the previous section, we summed up the data with same $\delta\phi$ (where $\delta\phi = \phi$ modulo(cell size)) values, to compute a parabolic correction function and a local ϕ modulation correction function (see section 4.3.2).

Applying that correction to the data, we end up with signal fluctuations inside $\pm$ 2% (see Fig 21) for the two different ϕ lines at N_η=7 and 15. These fluctuations do not look like cell to cell variations. The source of this non-uniformity is studied in section 4.6.

The resolution obtained for this set of cells, which corresponds to 30 000 events, is equal to 1.1 %. Subtracting from that value the measured contribution of the sampling term (0.62%) and noise term (0.17%) at 300 GeV, we obtain a constant term of 0.88 % along ϕ.

If we exclude a known bad region of the Endcap prototype (ϕ=[2-3], with larger thicknesses of the absorber plates (see section 4.6)), those numbers become : 0.91% for the resolution and 0.64% for the constant term along ϕ.

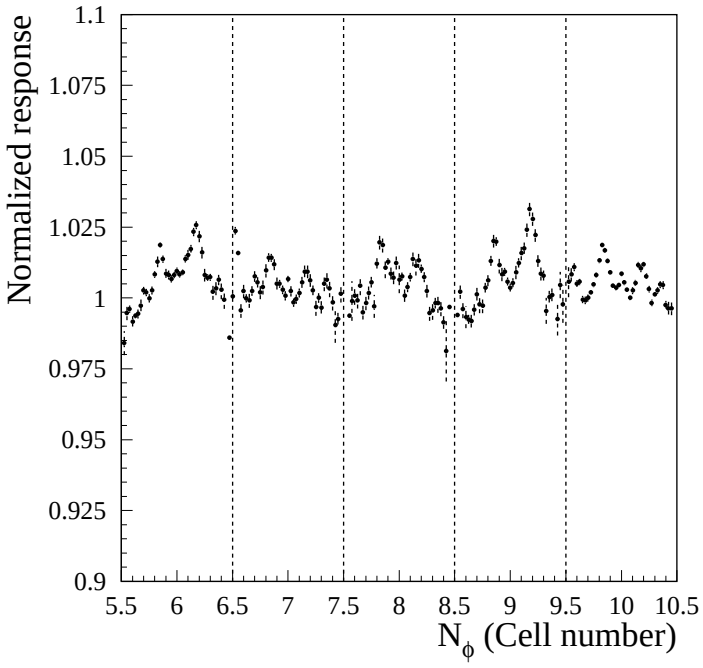

Figure 20: *Calorimeter response (normalized to the beam energy) showing ϕ modulations along five consecutive cells as measured for 300 GeV incident electrons.*

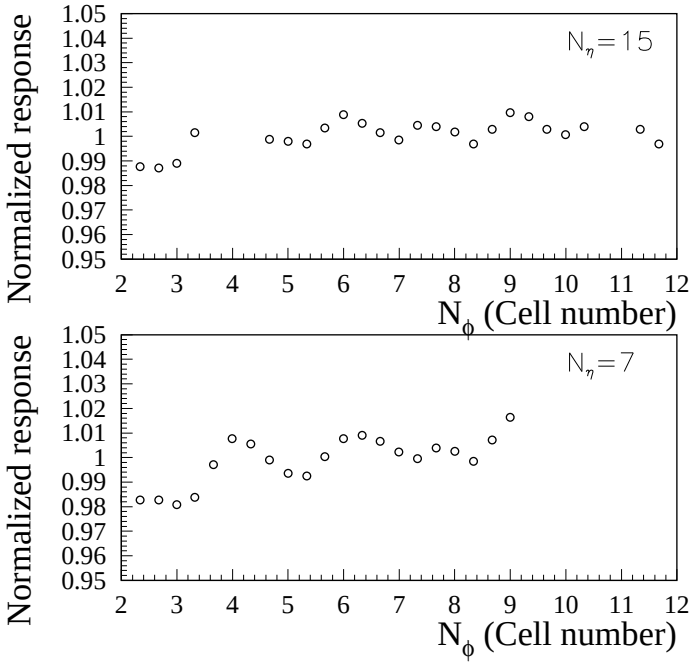

Figure 21: *Fluctuations along the ϕ direction of the normalized energy response for two values in η, after correction for the ϕ modulations.*

4.5.3 Global Response Uniformity

An overall energy resolution using a global parabolic and ϕ modulation correction function (see previous sections) is computed for the set of 48 cells mentionned in section 4.5.1, which corresponds to about 100 000 events over an area of $16(\eta) \times 3(\phi)$ cells. The distribution is shown on Fig 22 and has a relative dispersion of 1.14% (gaussian fit). Subtracting from this resolution value the measured contribution of the sampling term (0.76%) and noise term (0.26%) at 200 GeV, we obtain a global constant term of $0.79(\pm.04)\%$. This global constant term is slightly higher than the quadratic sum of the cell to cell dispersion (0.55%), illustrated in Fig. 19, and the local constant term (0.35%) obtained from the energy resolution fit (see section 4.3.4). This difference can be attributed to an additionnal non-uniformity in the ϕ direction (which did not appear in the local constant term because of the use of a local function of correction for the ϕ modulation in the energy resolution determination, see section 4.3.2).

The constant term computed with only three line in the ϕ direction is slightly optimistic. One can try to estimate a constant term over a large area in both the η and the ϕ directions by adding quadratically the constant term along η (0.66%) and along ϕ (0.64%) : it would result in a constant term of 0.92% but such a number should be taken as an upper limit on the constant term as correlations exists between the two directions.

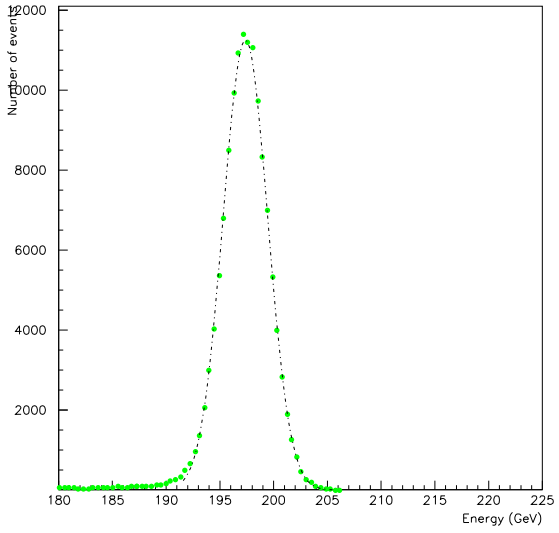

Figure 22: *Global energy response over 48 cells. Gaussian fit (dotted line) gives a resolution of 1.14%*

4.6 Non-uniformity analysis

We have investigated possible sources of non-uniformity using different measurements we did on both the electronics and the mechanical components of the prototype.

For the mechanical uniformity test, we have measured the capacitance values kapton per kapton over the complete prototype. Indeed, the capacitance of the kapton boards are

directly related to the (bi)gap between a kapton and the two adjacent lead plates so that a small displacement ϵ of the gap gives rise to a signal deviation of $\epsilon/3$ (see [3]).

We compared the capacitance measurements along ϕ with the data for two different η values and found some correlations between the capacitance and the signal values (more than 70% of correlation if we exclude the cells N_ϕ=2,3 and 5 where additional non-uniformity is suspected, see Fig. 23), so that we explain the main part of the ϕ non-uniformity by some deformations of the prototype structure along that direction. We measured a dispersion of the capacitance values of 2.6 % (rms) which contributes for 0.3% to the signal resolution ([5]). We can also mention that cell to cell variations of the local ϕ modulations, which were observed in the data (see Fig. 20 and the cell N_η = 22 used for the energy resolution computation Fig. 8), can be attributed to some displacements of the accordion structure (Such variations are well reproduced with the Monte Carlo simulation).

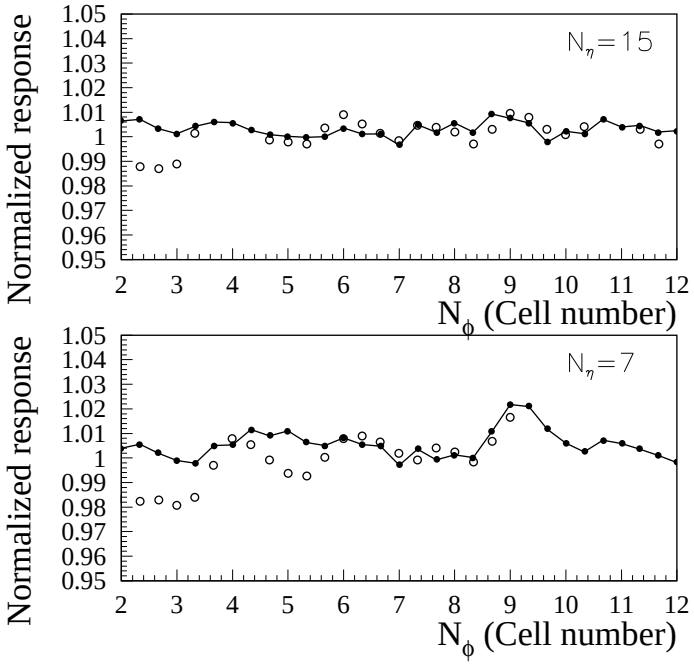

Figure 23: *Measured response variation in the ϕ direction and corresponding expected signal variation (i.e. ϵ/3) from capacitance measurements (broken line).*

There are several reasons which can cause these small deformations of the mechanical part. First, the prototype was dismantled in order to change kapton boards and we should mention here that the capacitance measurements of the gaps carried out on the prototype before its dismantling, showed a much more uniform mechanical structure. Another reason is that the detector was moving in azimuthal direction during the tests.

Obviously, special care has to be taken in all such operations in order to keep the detector structure sufficiently rigid.

An another source of non-uniformity is illustrated in Fig 24 and corresponds to the lead thickness variations. As mentioned in section 4.5.2, there is a region at small ϕ values (ϕ=[2-3]) where the lead thickness is larger. The corresponding decrease (1-2 %) in the energy response, due to this excess of lead, is visible on Fig. 23.

The contribution of the lead thickness variation to the signal dispersion was estimated to be 0.3 % excluding the two layers ϕ=[2-3] and 0.55 % over the full prototype range ϕ=[2-12] (This contribution of the lead thickness variation has been estimated to be the dispersion of the absorber (grouped by three, i.e. one cell) weights, close to the result of [5]).

We found a large correlation (60%) between the capacitance values of the cell readout channels and the η structures present in the data (Fig. 19). This is shown in Fig. 25 where for a given ϕ value, we have plotted, as a function of the η cell number, the capacitance values of the first sampling (normalized to the mean value of the capacitance) and the energy response as obtained from the first sampling for 200 GeV incident electrons. Most of these structures are reproduced by mother board capacitance values distribution.

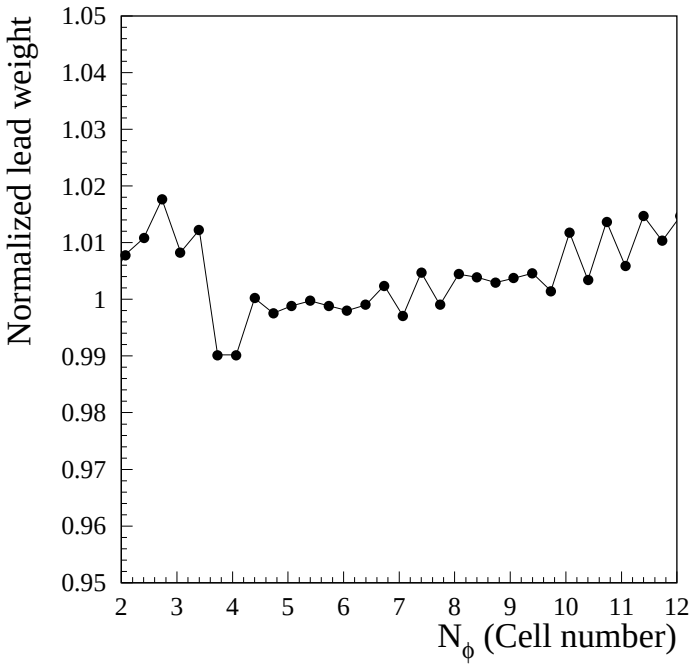

Figure 24: *Lead weight variation (i.e. close to lead thickness variation) versus ϕ (cell number).*

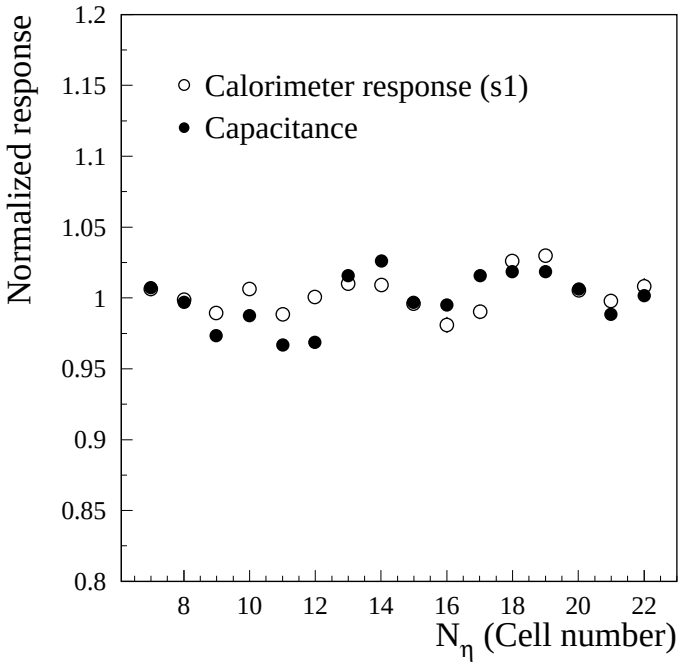

Figure 25: *Normalized energy response of the first sampling along the η direction (open circle) and mother board capacitances (black point) of that sampling.*

The distribution of the cell response along the η direction has an rms of 0.5 %. Therefore we estimated a contribution of 0.3% to this number related to the capacitance values.

Finally, the various sources of non-uniformity are summarized in the following table 3. For the calibration contribution, we have taken the estimation coming from the barrel prototype [3].

Effect	contribution (%)
Electronics	
Calibration	0.35
capacitance	0.3
Mechanics	
residual Φ-modulation	0.35
gap non-uniformity	0.3
absorber thickness	0.3 (0.55)
total ($\oplus$)	0.72 (0.85)

Table 3: *The different contributions to the constant term. Numbers in parenthesis have been obtained including also the ϕ=[2-3] layers with heavy absorbers*

If we compare the expected constant term from table 3 : 0.72% and the constant term extracted from the scan data, i.e. 0.79($\pm$.04) (estimated $<$ 0.9% for a larger area), we can conclude that a large part of the constant term can be attributed to known instrumental effects.

5 Conclusions

The measured performances of the Endcap prototype are very close to the one obtained for the barrel in terms of resolution and linearity. This confirms that one can adapt the accordion geometry to an Endcap configuration without significant loss in the performances. The constant term over a large area has been found somewhat larger. The sources of non-uniformities point mainly to mechanical effects (gap width, lead thickness) and to capacitive effects. Increased caution during detector fabrication and assembly should allow to reach an uniformity of 0.5 %.

References

[1] ATLAS Collaboration, Letter of Intent, CERN/LHCC/92-4 (1992).

[2] ATLAS Collaboration,Technical Proposal, CERN/LHCC/94-43 (1994).

[3] D.M.Gingricht et al. (RD3 Collaboration), Performance of a Large Scale Prototype of the ATLAS Accordion Electromagnetic Calorimeter, RD3 Internal Note 58, to be submitted to Nucl. Inst. and Meth.

[4] B.Aubert et al. (RD3 Collaboration), Status Report and further R&D for EM and Hadronic Calorimetry, CERN/DRDC/93-4 (1993).

[5] A.Cravero and F.Gianotti, Uniformity of response and energy resolution of a large scale prototype of the Barrel Accordion calorimeter, ATLAS Internal note CAL-NO-33 (1994).